Wavelength-dependent differences in photocatalytic performance between BiOBr nanosheets with dominant exposed (0 0 1) and (0 1 0) facets

Haiping Li[a], Tingxia Hu[b], Na Du[b], Renjie Zhang[b], Jianqiang Liu[c], Wanguo Hou[a,b,*]

[a] National Engineering Research Center for Colloidal Materials, Shandong University, Jinan 250100, PR China
[b] Key Laboratory for Colloid and Interface Chemistry (Ministry of Education), Shandong University, Jinan 250100, PR China
[c] School of Physics, Shandong University, Jinan 250100, PR China

ABSTRACT

BiOBr nanosheets with dominant exposed (0 1 0) facets exhibit higher photocatalytic activity than those with highly exposed (0 0 1) facets under illumination of light with wavelengths (λ) of $\sim$365 and $\geq$420 nm, but lower photoactivity under light with λ of 254 nm. The λ-dependent differences in photocatalytic activity result from different (0 0 1) facet exposure percentages ($F(0 0 1)$) and nanosheet thicknesses (H) between the two samples. Whether the difference in $F(0 0 1)$ or that in H influences the photoactivity of the BiOBr nanosheets as a primary factor depends on incident light penetration depth which increases with the λ. This study gives a better insight into the structure-performance relationship of two-dimensional (2D) photocatalysts and will supply important direction for photocatalytic studies of 2D semiconductors.

© 2016 Elsevier B.V. All rights reserved.

1. Introduction

Fossil fuels are indispensable in every aspect of our lives, but their nonrenewability and gradually reduced reserves have caused energy crisis, while their consumptions are accompanied with serious environmental contamination [1,2]. Semiconductor photocatalysis is currently considered a promising technology to solve these two problems by photosplitting water to generate H_2, photocatalytically reducing CO_2 to produce hydrocarbon fuels, and photodegrading toxic pollutants to remedy the environmental pollution [3–5]. TiO_2, as a nontoxic, chemically stable and widely available photocatalyst, attracted much attention of researchers before, but its incapability in absorbing visible light, resulting from its wide band gap ($\sim$3.2 eV), leads to a much low photocatalytic activity under sunshine irradiation, which limits its industrial application [4]. At present, numerous visible-light responsive photocatalysts have been synthesized, but their photocatalytic activity is still too low to satisfy the requirement of large-scale application, primarily because of high recombination rate of photogenerated charge carriers [6]. Improving the visible-light photocatalytic activity of semiconductor photocatalysts should be a priority currently.

Polar two-dimensional (2D) semiconductors possess natural superiorities as photocatalysts, such as high material utilization, [7] short transfer distances of charge carriers, [8,9] and self-generated internal electric fields (IEFs) which accelerate the separation of photoinduced charge carriers [10–13]. Bismuth-based Sillén-type semiconductors, such as BiOX (X = Br or I) [13–15], are one of the most studied kinds of polar 2D visible-light photocatalysts because of their relatively high photocatalytic activity. To further improve their photocatalytic performance, many ways were developed and studied, such as construction of 3D hierarchical structures, [14] elemental doping, [16,17] generation of surficial defects (e.g. oxygen vacancy), [15,18] fabrication of composites or heterojunctions, [19,20] and crystal facet engineering [21,22]. Recently, we found reducing the nanosheet thickness could also improve the photocatalytic activity of BiOBr nanosheets [8,9]. Actually, systematical studies on structure-performance relationships of the BiOX photocatalysts are necessary so as to synthesize high efficient products. Nonetheless, even though so many mays have been verified to be capable of improving the photocatalytic activity of BiOX, to our knowledge, research about the influence of incident light wavelength (λ) on these ways has not been reported yet.

* Corresponding author at: National Engineering Research Center for Colloidal Materials, Shandong University, Jinan 250100, PR China.
E-mail address: wghou@sdu.edu.cn (W. Hou).

In this study, the photocatalytic activity of BiOBr nanosheets with dominant exposed (0 0 1) and (0 1 0) facets (denoted as B001 and B010) were investigated systematically. The B010 exhibits higher photocatalytic efficiency than the B001 under visible light with λ of ≥420 nm, and ultraviolet light with λ of ~365 nm, but lower efficiency under light with λ of 254 nm. The λ-dependent differences in the photoactivity are attributed to the differences in the nanosheet thicknesses and (0 0 1) facet exposure percentages of the two BiOBr nanosheets. This work provides significant direction for preparation and studies on photoactivity of 2D photocatalysts.

2. Experimental

2.1. Materials

Bi(NO$_3$)$_3$·5H$_2$O, NaBr, KCl and NaOH were purchased from Aladdin (Shanghai, P. R. China). Ultrapure water used in this study was obtained from a Hitech-Kflow water purification system (Shanghai, P. R. China).

2.2. Preparation of BiOBr and BiOCl nanosheets

BiOBr and BiOCl nanosheets were prepared according to the literature with a little modification [23]. In a typical procedure, 4 mmol of Bi(NO$_3$)$_3$·5H$_2$O and 4 mmol of NaBr or KCl were added into 60 mL distilled water at room temperature with continuous stirring, and then the pH of the suspension was adjusted to 6.0 with 1 M NaOH solution. After stirring for 30 min, the mixture was poured into an 80-mL polytetrafluoroethylene-lined stainless auto-clave, heated at 160 °C for 24 h under autogenous pressure, and then cooled to the room temperature. The resulting precipitates were collected by filtration, washed with water thoroughly and dried at 60 °C. The product obtained was denoted as B010 or C010. The product obtained at the similar conditions without the pH adjustment was denoted as B001 or C001.

2.3. Characterizations

Powder X-ray diffraction (XRD) was performed on a X'Pert Pro MPD X-ray diffractometer (Philips, Holland), with Cu Kα radiation (λ = 1.54184 Å) generated at 40 mA and 40 kV, and a scanning rate of 1/min. X-ray photoelectron spectroscopy (XPS) was carried out on a Thermo Scientific Escalab 250Xi spectrometer (UK) with Al Kα radiation. The C 1s peak at 284.6 eV was used to calibrate peak positions. Electron paramagnetic resonance (EPR) spectra were recorded on a Bruker A300-10/12 spectrometer (Germany) at temperature of 100 K. Morphology observations were performed on a Supra55 field emission-scanning electron microscope (SEM, Zeiss, USA) and a JEM-2100F transmission electron microscope (TEM, Jeol, Japan). Selected area electron diffraction (SAED) patterns were obtained from the TEM. UV–vis diffuse reflectance spectra were obtained using a U-4100 spectrophotometer (Hitachi, Japan), with a BaSO$_4$ reference. Photoluminescence (PL) spectra were measured using an F-7000 spectrophotometer (Hitachi, Japan) with excitation wavelengths of 240–420 nm, and excitation and emission slit widths of 5 nm. Specific surface areas were probed by measuring volumetric N$_2$ adsorption-desorption isotherms at liquid nitrogen temperature on a Quantachrome NOVA2000E instrument (USA). Samples were degassed at 120 °C for 6 h under vacuum before measurements. Photocurrent density was measured on an electrochemical workstation (Gamry Reference 600, USA) with a standard three-electrode cell. Ag/AgCl and Pt wire were used as the reference and counter electrodes, respectively, with 0.5 M Na$_2$SO$_4$ as the electrolyte solution and applied bias of −0.5 eV. The working electrodes were prepared by coating the sample slurries (obtained by grinding the mixture of 0.02 g of BiOBr, 40 μL of PEDOT-PSS (Sigma, 1.3%)

and 200 μL of H$_2$O) onto a clean indium doped tin oxide (ITO) glass surface, followed by vacuum drying for 3 h. A 15-W mercury lamp (λ = 420 nm) and a 300-W xenon lamp equipped with an ultraviolet cutoff filter (λ ≥ 420 nm) were used as the ultraviolet and visible light sources.

The photocatalytic activity of as-prepared photocatalysts was evaluated by degrading salicylic acid (SA) at the room temperature, on a XPA-7 photocatalytic reaction apparatus (Xujiang Electromechanical Plant, Nanjing, P.R. China) [9,24]. A 400-W metal halide lamp equipped with an ultraviolet cutoff filter (λ ≥ 420 nm) was used as the visible light source. A 15-W mercury lamp with λ of 254 nm and a 300-W and a 15-W mercury lamps (~300 nm < λ < 580 nm, with maximum emission λ of ~365 nm) equipped with a visible cutoff filter (λ ≤ 365 nm) were used as the ultraviolet sources. For simplicity, the four light sources were marked as VL420, UV254, UV365^H, and UV365^L, respectively. For each run, 0.05 g of photocatalyst was added to 50 mL of SA solution (20 mg/L). Prior to irradiation, the suspension was stirred in the dark for 1 h to ensure sorption equilibrium. After a given irradiation time, ~4 mL of dispersions were taken out and filtered through 0.45-μm poly(ether sulfone) syringe filters. The absorbance of filtrates was measured by a Hewlett-Packard 8453 UV–vis spectrophotometer (USA) at λ of 296 nm. The ratio of remaining SA concentration to its initial concentration, C/C_0 was equal to the ratio of corresponding absorbances.

3. Results and discussion

3.1. Photocatalytic activity

The SA was chosen as the photodegradation substrate to evaluate the photocatalytic activity of the BiOBr nanosheets. One reason is that the SA almost shows no absorption under the VL420 and UV254 irradiations (Fig. S1, Supporting information), indicating that photosensitizing effect on the photodegradation process is negligible. The other reason is that the adsorption capacities of the SA on the BiOBr nanosheets and the adsorption capacity difference between the B001 and B010 are all minor (Fig. S2, Supporting information), and thus the effect of the adsorption capacity difference on the photoactivity of the samples is also negligible. Meantime, the difference in photosensitizing effect between the B001 and B010 can be neglected because the photosensitization effect depends on the adsorption capacity of photosensitizers [23].

Fig. 1 shows the photodegradation of SA on the BiOBr nanosheets under the VL420, UV365 (UV365^H and UV365^L) and UV254 irradiations. The absorbance of pure SA hardly varies during the entire illumination process, indicating negligible self-photodegradation of SA. Under the VL420 and UV365 irradiations, the B010 exhibits higher photocatalytic efficiencies than the B001. The former can degrade ~82% of the SA in 35 h under the VL420 irradiation, ~97% in 4 h under the UV365^H irradiation, and ~17% in 74 h under the UV365^L irradiation, while the latter degraded ~41, 79, and 13%, respectively (Fig. 1a–c). However, under the UV254 irradiation, the photocatalytic efficiency of the B010 is lower than that of the B001. The B010 degrades only ~18% of the SA in 86 h, while the B001 can degrade ~25% (Fig. 1d). Superoxide radicals are primary active species in the photodegradation processes [9]. To quantitatively compare the photocatalytic efficiencies of the BiOBr samples, the photodegradation data were fitted to a pseudo-first-order kinetic model, $-\ln(C/C_0) = kt$ where k and t are the apparent first-order rate constant and the degradation time, respectively. (Fig. S3, Supporting information). The k values of the B010 are ~3.0, 2.0, 1.4, and 0.7 times those of the B001 under the VL420, UV365^H, UV365^L, and UV254 irradiations, respectively (Fig. 1e). The ratios of k(B010) to k(B001) decrease gradually with reduction of the λ. This
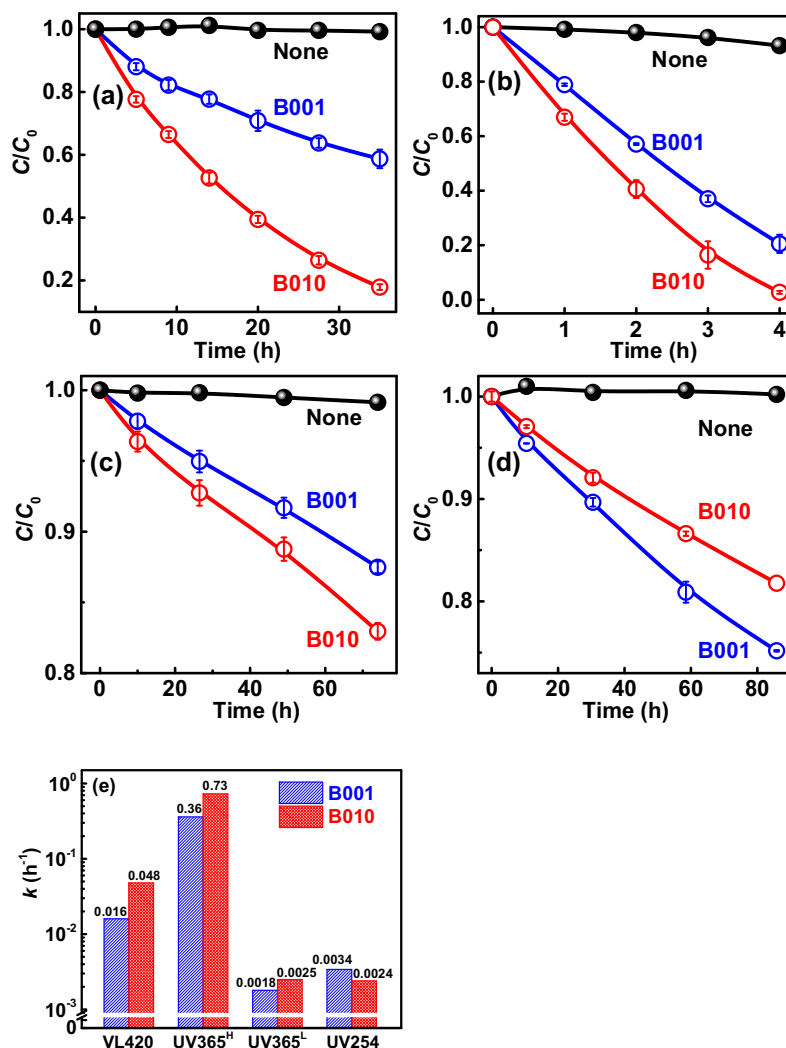
Fig. 1. Photocatalytic degradation of SA on BiOBr nanosheets under VL420 (a), UV365[H] (b), UV365[L] (c) and UV254 (d) irradiations, and relative pseudo-first-order kinetics rate constant (e). VL420, visible light from 400-W metal halide lamp equipped with an ultraviolet cut-off filter ($\lambda \geq 420$ nm); UV365[H] and UV365[L], ultraviolet light from 300 and 15-W mercury lamps equipped with a visible cut-off filter ($\lambda \leq 365$ nm), respectively; UV254, ultraviolet light from a 15-W mercury lamp ($\lambda = 254$ nm).

λ-dependent differences in the photoactivity between the B010 and B001 have not been reported so far. We also investigated the photocatalytic degradation of 2,4-dichlorophenol on the B001 under the VL420 irradiation, but no obvious degradation was observed in 10 h (Fig. S4, Supporting information).

3.2. Structures and physicochemical properties of BiOBr nanosheets

To well clarify the mechanism of above λ-dependence of the photoactivity differences, structures and physicochemical properties of BiOBr nanosheets are characterized in detail.

XRD patterns of the B001 and B010 [9] shown in Fig. 2 exhibit similar diffraction peak positions corresponding to a pure tetragonal phase of BiOBr (JCPDS file No. 73–2061). The (0 0 1) peaks of the B010 are much weaker than those of the B001. As shown in the inset, the intensity ratios of (0 1 2), (1 1 0) and (0 2 0) to (0 0 1) peaks of the B001 are all conspicuously <1, while those of the B010 are all >1, demonstrating that the B001 and B010 probably expose dominantly the (0 0 1) and (0 1 0) facets, respectively, in consistence with of Lin and coauthors' results [25].

To confirm elemental compositions and surficial structures of the BiOBr nanosheets, XPS spectra of the samples (Fig. 3) were

measured. The survey spectra (Fig. 3a) show that the B001 and B010 comprise the same elements (Bi, Br, O and adventitious C [26]). The high-resolution XPS spectra of Bi 4f (Fig. 3b) and Br 3d (Fig. 3c) were accurately deconvoluted into two peaks corresponding to Bi $4f_{5/2}$ and $4f_{7/2}$ at binding energies (BE) around 164.6 and 159.3 eV, and Br $3d_{3/2}$ and $3d_{5/2}$ at BE of 69.4 and 68.3 eV, which are related to the
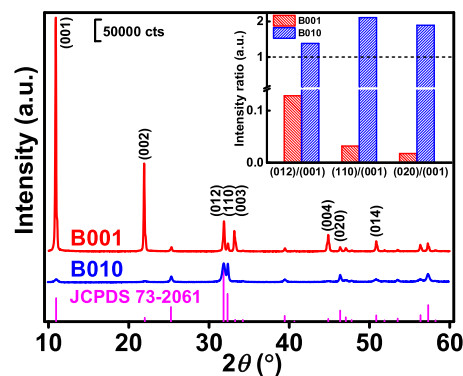
Fig. 2. XRD patterns of BiOBr nanosheets. Inset is the intensity ratios of (0 1 2), (1 1 0) and (0 2 0) to (0 0 1) peaks.
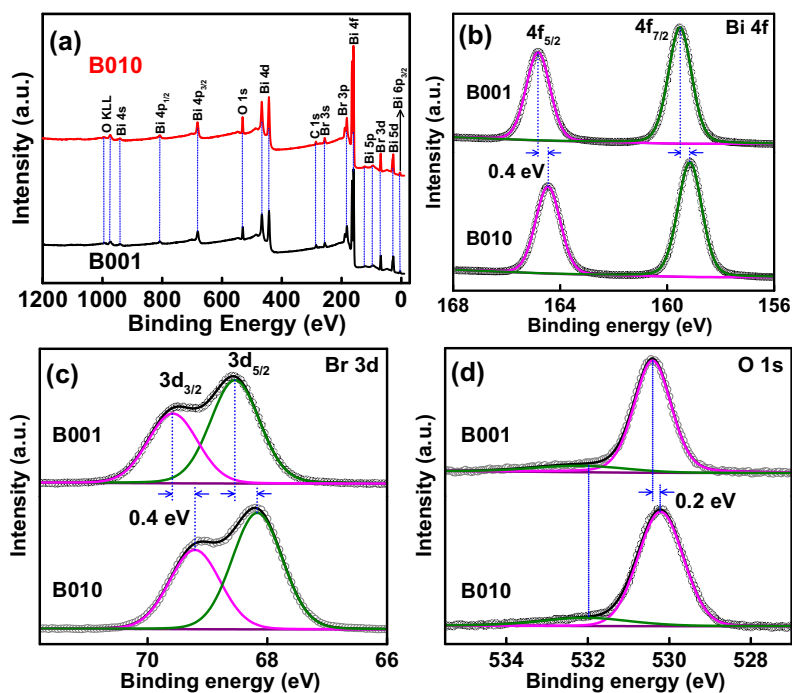
Fig. 3. XPS survey spectra (a) and high-resolution XPS spectra of Bi 4f (b), Br 3d (c) and O 1s (d) regions of BiOBr nanosheets.

Bi^{3+} and Br^- in BiOBr, respectively [8,27]. Peaks of oxygen vacancy [8,28,29] are not observed, and the EPR spectra of the samples also show no peaks [21] (Fig. S5, Supporting information), suggesting the influence of oxygen vacancies is negligible. The peak BE of Bi 4f and Br 3d for the B010 are all ~0.4 eV lower than those for the B001, as shown by the dotted lines (Fig. 3b and c). The O 1s high-resolution XPS spectra of both the B001 and B010 (Fig. 3d) were deconvoluted into two peaks. Peaks at BE around 530.3 eV are ascribed to the O^{2-} in BiOBr. The peak BE of the B001 is ~0.2 eV higher than that of the B010, as shown by the dotted lines. Peaks at BE around 531.9 eV correspond to hydroxyl or H_2O on BiOBr surfaces [8,27].

On the whole, the BE of Bi 4f, Br 3d and O 1s peaks of the B010 are all lower than those of the B001. As reported, the increase/decrease in surficial electron density could decrease/increase the BE [30–32]. Therefore, the surficial electron density of the B010 is higher than that of the B001 or further that the (010) facet possesses higher electron density than the (001) facet for the BiOBr nanosheets. This is presumably because the (010) facet possesses lower surficial energy than the (001) facet [33].

Morphologies of the B001 and B010 were observed by the SEM and TEM. SEM and TEM images show that both the B001 and B010 are irregular nanosheets (Fig. 4a and d), which agrees with reported results [25]. High resolution TEM (HRTEM) image of the B001 (Fig. 4b) shows two perpendicular sets of lattice fringes with spacings of 0.277 nm (Fig. 4e), corresponding to (110) and (1–10) planes both of which are perpendicular to the (001) plane. The SAED pattern of the B001 (Fig. 4c) shows clear ordered diffraction spots, indicating a single crystal structure and all the diffraction planes are perpendicular to the (001) plane. The HRTEM image of the B010 (Fig. 4e) shows three sets of lattice fringes with angles of 88.2, 45.9 and 45.9° and spacings of 0.201, 0.281 and 0.281 nm, respectively, corresponding to (004), (102) and (−102) planes which are vertical to the (010) plane. The SAED pattern of the B010 (Fig. 4f) also shows a single crystal structure and all the diffraction planes are vertical to the (010) plane. Since it's difficult to differentiate the SAED patterns of B001 and B010, we superimposed these two patterns together and a difference is clearly observed (Fig. S6, Supporting information). Based on the above results, it's

concluded that the B001 nanosheets expose (001) facets on both the top and bottom surfaces and (010), (110) and (100) facets on the lateral surfaces (Fig. 4g), while the B010 nanosheets expose (010) facets on both the top and bottom surfaces and (001), (102) and (100) facets on the lateral surfaces (Fig. 4i), which is in accordance with Lin and coauthors' results [25]. Average lateral sizes (L) and thickness (H) of the B001 are ~2092 and 173 nm, respectively (Fig. S7, Supporting information), while those of the B010 are ~134 and 44 nm, [9] respectively. Provided the top and bottom planes of the BiOBr nanosheets are circular or square, the percentages (F) of exposed (001) facets for the B001 and exposed (010) facets for the B010 were calculated to be ~86 and 60%, respectively, using the equation $F = 1/(1 + 2H/L)$.

Photoabsorption performance of semiconductors affects prominently their photocatalytic activity [34]. UV–vis diffuse reflectance spectra (Fig. 5a) show that the B001 and B010 exhibit similar photoabsorption range and intensity, in accordance with reported results [25]. Band gaps (E_g) of the BiOBr nanosheets were determined using equation $\alpha h\nu = A(h\nu - E_g)^{n/2}$ where h, α, ν and A are the Planck constant, the absorption coefficient, the light frequency and the proportionality constant, respectively. n decides characteristics of the transition in a semiconductor, i.e. n = 1 for a direct bandgap transition and n = 4 for an indirect bandgap transition [24]. n = 4 is suitable for both the B001 and B010. The B001 and B010 have similar E_g, ~2.77 eV which is close to the reported values [8,9,35]. To confirm energy band positions, valence band (VB) XPS spectra of the B001 and B010 were measured. As shown in Fig. 5b, the distance (E_{VB}) from VB maximum to Fermi level [36] for the B001 and B010 is 2.32 and 1.91 eV, respectively, and the corresponding conduct band (CB) edges (E_{CB}, distance from CB minimum to Fermi level) were calculated to be −0.45 and −0.86 eV using the equation $E_{CB} = E_{VB} - E_g$. Clearly, the Fermi levels of both the B001 and B010 lies closer to the CB than to the VB, which agrees well with the reported result [37]. These reveal that BiOBr is an n-type semiconductor here [36,38] though it's generally considered as a p-type one [14,39,40].

The specific surface area of a semiconductor is another import factor influencing the photocatalytic performance [41]. N_2
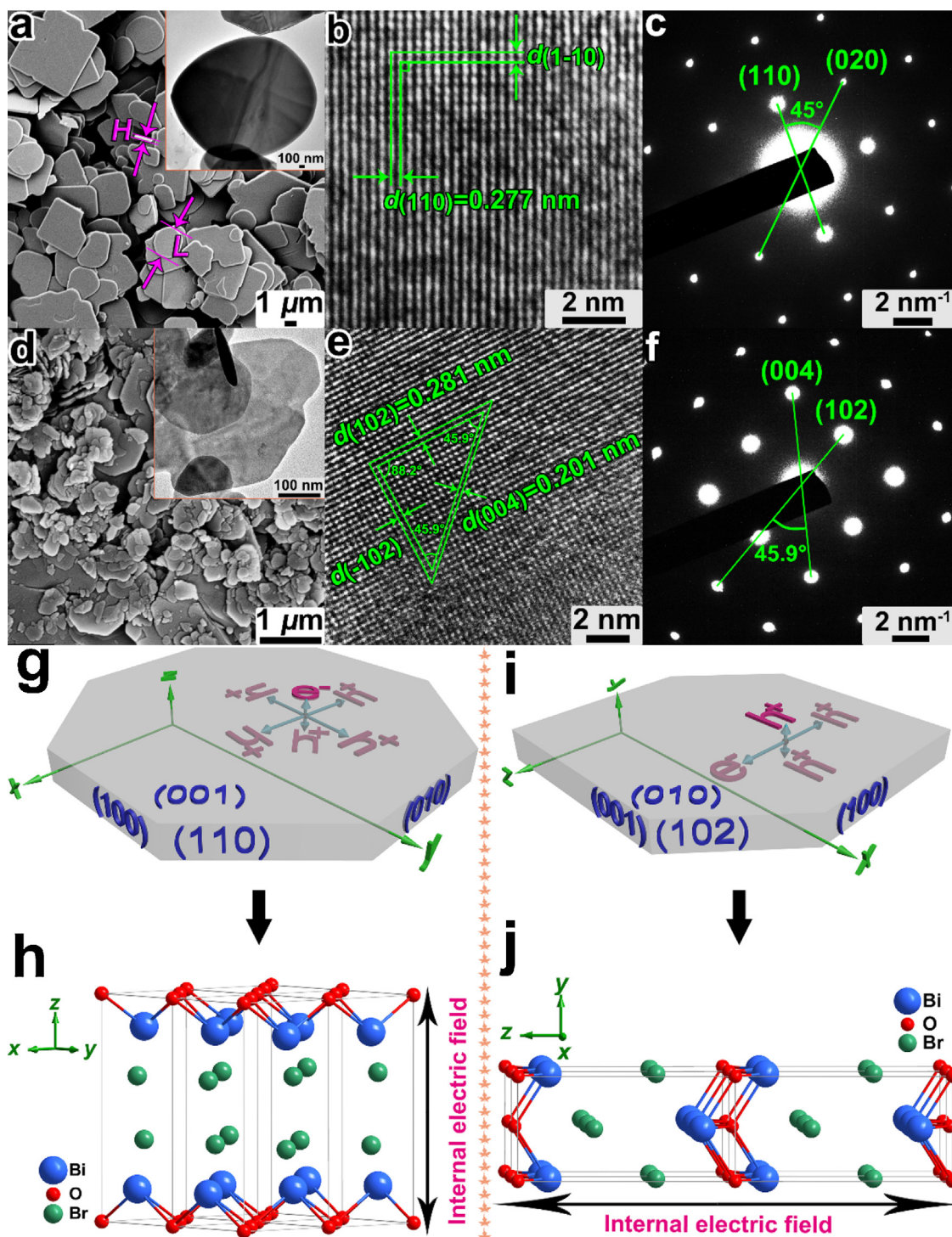
Fig. 4. SEM (a and d), TEM (insets in a and d), HRTEM (b and e) and SAED (c and f) images and schematic illustrations of nanosheet (g and i) and crystal lattice (h and j) structures of B001 (a–c, g and h) and B010 (d–f, i and j).

sorption isotherm measurement was performed to obtain the specific surface areas and pore structures of the BiOBr samples (Fig. 5c). The Brunauer–Emmett–Teller (BET) specific surface areas (S_{BET}) of the B001 and B010 are 7.0 and 16.4 m^2/g, respectively. Their isotherms are of type IV and hysteresis loops are of type H4 and H3, respectively, indicating the existence of slit-shaped mesopores [42,43] which were formed by the aggregation of BiOBr nanosheets. The pore size distributions (Fig. 5d) calculated by the Barrett–Joyner–Halenda (BJH) method indicate that the average mesopore sizes of the B001 and B010 are ∼2.3 and ∼2.9 nm,

respectively. The B010 possesses much higher S_{BET} [25] and slightly larger pore size than the B001.

3.3. Mechanism for λ dependence of differences in photocatalytic performance

The B001 and B010 show similar photoabsorption capability (Fig. 5a) and the light sources UV365^L and UV254 provide similar light intensity, indicating negligible effects of the photoabsorption and light intensity on the differences in photocatalytic
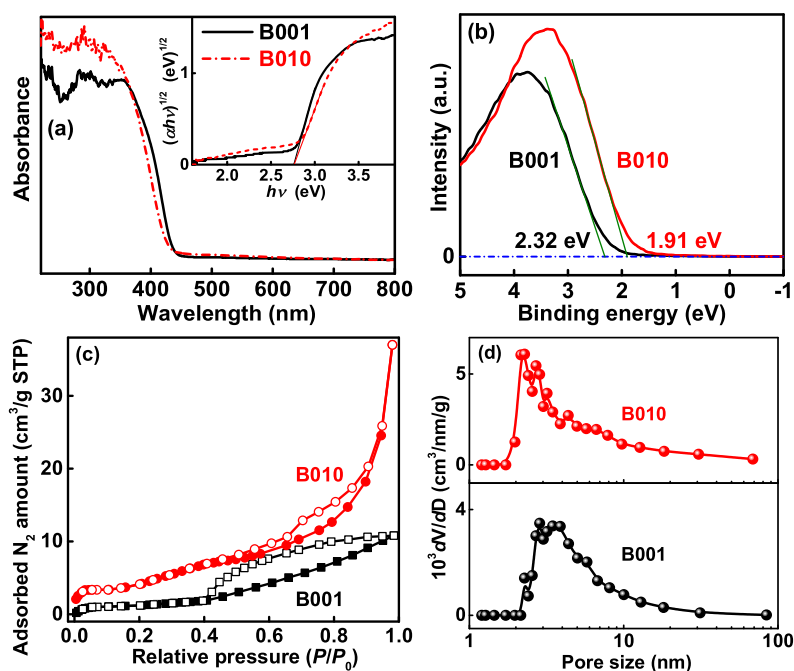
Fig. 5. UV–vis diffuse reflectance (a) and valence band XPS (b) spectra, N_2 sorption isotherms (c) and pore size distribution curves (obtained from adsorption branch) (d) of BiOBr nanosheets. Inset in (a) is $(\alpha h\nu)^{1/2}$ vs. $h\nu$ curves. The Fermi level is located at 0 eV [38] in (b).

activity between the B010 and B001. Though the B010 possesses higher surficial electron density and E_{CB} which contribute to higher photoactivity, than the B001, we think these differences are independent of the λ and thereby are unrelated to the photoactivity differences. The S_{BET} value of the B010 is more than two times that of the B001, suggesting the S_{BET} is probably an important factor influencing the photoactivity. This can be further verified by that the k values normalized by the S_{BET} (k') for the B010, 44.5 mg h^{-1} m^{-2}, is less than that for the B001, 51.4 mg h^{-1} m^{-2}, under the UV365^H irradiation. However, k' for the B010, 2.92 mg h^{-1} m^{-2}, is still larger than that for the B001, 2.30 mg h^{-1} m^{-2}, under the VL420 irradiation, and the S_{BET} difference shouldn't depend on the λ, so the S_{BET} difference is not the key factor.

The recombination efficiency of photogenerated charge carriers (REPC) can affect fundamentally the photocatalytic performance of semiconductor photocatalysts [44,45]. PL intensity and photocurrent density of photocatalysts are capable of indirectly characterizing the REPC [15,44,45]. The PL spectra of the B001 and B010 at different excitation wavelengths (λ_{ex}) show that the PL intensity of the B010 is lower than that of the B001 at $\lambda_{ex} > 320$ nm, revealing a lower REPC, but is higher at $\lambda_{ex} < 260$ nm, meaning a higher REPC (Fig. 6). Photocurrent density of the BiOBr samples under ultraviolet ($\lambda = 254$ nm) and visible light ($\lambda \geq 420$ nm) irradiations is shown in Fig. 7. The B010 exhibits a lower photocurrent density than the B001 under the ultraviolet light, revealing a higher REPC, and a higher photocurrent density under the visible light,

indicating a lower REPC, which is in accordance with the results of PL spectra at $\lambda_{ex} < 260$ nm and >320 nm, respectively. These suggest that the λ-dependent differences in the photoactivity arise from the λ-dependent differences in the REPC.

The REPC of photocatalysts is affected by many factors, such as the particle size, [46] IEF, [10,11] oxygen vacancy, [47] and composite/heterojunction [48]. For the BiOBr nanosheets, on the one hand, the layered structure provides an adequately large space to polarize related atoms and orbitals. The induced dipole between $[Bi_2O_2]^{2+}$ and Br^- slabs brings about an IEF along the z-axis (Fig. 4h and j) which accelerates the separation and transport of the photogenerated electrons (e^-) and holes (h^+) (Fig. 4g and i), and thus lowers the REPC [12]. Increase of the $F(0\,0\,1)$ is favorable for intensification of the IEF effect and enhancement in the photoactivity [13,23]. The higher photoactivity of the B001 than that of the B010 under the UV254 irradiation is attributed to the IEF effect because the $F(0\,0\,1)$ of the B001 ($\sim$86%) is much greater than that of the B010 ($\ll$40%). On the other hand, the REPC can be lowered by reduction of the H of nanosheets which decreases transfer distances of the photogenerated e^- and h^+ (Fig. 3g and i) [8,9]. This can explain why the B010 exhibits higher photoactivity than the B001 under the VL420 irradiation, in view of the quite less H of the B010 ($\sim$44 nm) than that of the B001 ($\sim$173 nm). Herein, a question comes into being: why do the $F(0\,0\,1)$ and H have "λ-dependent" effects on the photoactivity?

Optical penetration depth (OPD) in semiconductors affects the activity of photocatalysts [49,50]. The OPD increases with lengthening λ according to the equation OPD $= \lambda/(4\pi K)$ where K is the
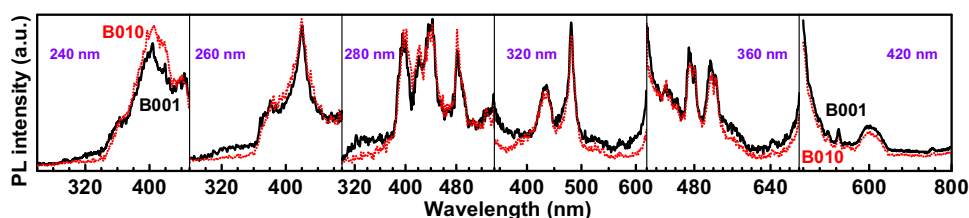
Fig. 6. Photoluminescence (PL) spectra of BiOBr samples with excitation wavelengths (λ_{ex}) of 240, 260, 280, 320, 360 and 420 nm.
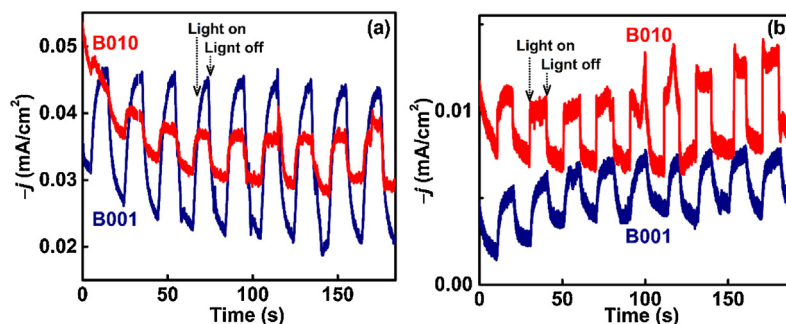
Fig. 7. Photocurrent density under irradiation of a 15-W mercury lamp ($\lambda = 254$ nm) (a) and a 300-W xenon lamp equipped with an ultraviolet cut-off filter ($\lambda \geq 420$ nm) (b) for BiOBr nanosheets.

extinction coefficient [51] which varies with changes of λ and material structures [52–55]. Generally, the K lies between 0 and 1 and gradually decreases with increasing λ at $\lambda > 350$ nm, but at $\lambda < 350$ nm, the K is probably >1 for some semiconductors [53,54]. The OPD of the VL420 (>∼$33/K$ nm) in BiOBr nanosheets are probably >$H/2$ of B010 (∼22 nm), or the K is <1.5. In this case, the shortest transfer distances of photoinduced e^- and h^+ from the inside to the surface of nanosheets are the $H/2$ of B010, no matter whether the OPD is greater than the $H/2$ of B001 or not (Fig. 8a). Under this circumstance, the H difference have greater effect on the REPC than the $F(0\,0\,1)$ difference between the B010 and B001, resulting in the higher photoactivity of B010 (Fig. 1a, b and d). However, the OPD of the UV254 (∼$20/K$ nm) is probably <$H/2$ of B010, or the K is >0.9. In this case, the shortest transfer distances of e^- and h^+ from the inside to the surface of nanosheets are the OPD (Fig. 8b), and the influence of the H difference on the REPC is weaker than that of the $F(0\,0\,1)$ difference, which leads to higher photoactivity of the B001 (Fig. 1c and d). Herein, the speculation on the K values is reasonable according to the literature, but we are unable to determine the accurate values under our present experimental conditions. The PL spectra (Fig. 6) probably indicate that the H difference has a greater effect at $\lambda > 320$ nm but a less one at $\lambda < 260$ nm than the $F(0\,0\,1)$ difference.

For comparison, the BiOCl nanosheets with highly exposed $(0\,0\,1)$ and $(0\,1\,0)$ facets (denoted as C001 and C010) were also prepared according to the literature [23]. Differences between their XRD patterns (Fig. S8, Supporting information), morphologies (Fig. S9, Supporting information), UV–vis diffuse reflectance spectra (Fig. S10a, Supporting information) and SA adsorption capacities (Fig. S11, Supporting information) are similar to the reported results [23] and those between the B010 and B001, but the C001 and C010 possess similar surficial electron density (Fig. S12, Supporting information), closer energy band levels (Fig. S10b), and larger H (∼195 nm for the C001 and ∼96 nm for the C010, Fig. S9) as/than the B010 and B001. The C001 exhibits higher photoactivity than the C010 under whether the UV365[H] or the UV254 irradiation (Fig. S13, Supporting information), which is different from the BiOBr nanosheets. This probably because the $H/2$ of C001 and C010, ∼97 and 48 nm are both larger than the OPDs of UV365[H] and UV254, meaning the influence of the H difference is weaker than that of the $F(0\,0\,1)$ difference here.

4. Conclusions

The B001 with highly exposed $(0\,0\,1)$ facets and the B010 with dominant exposed $(0\,1\,0)$ facets were synthesized. The L, H, $F(0\,0\,1)$ and S_{BET} are ∼2092 nm, ∼173 nm, ∼86% and 7.0 m^2/g for the B001 and ∼134 nm, ∼44 nm, ≪ ∼40% and 16.4 m^2/g for the B010. The B010 possesses less H and $F(0\,0\,1)$ and larger S_{BET} than the B001. The XPS data indicate that the B010 possesses higher surficial electron
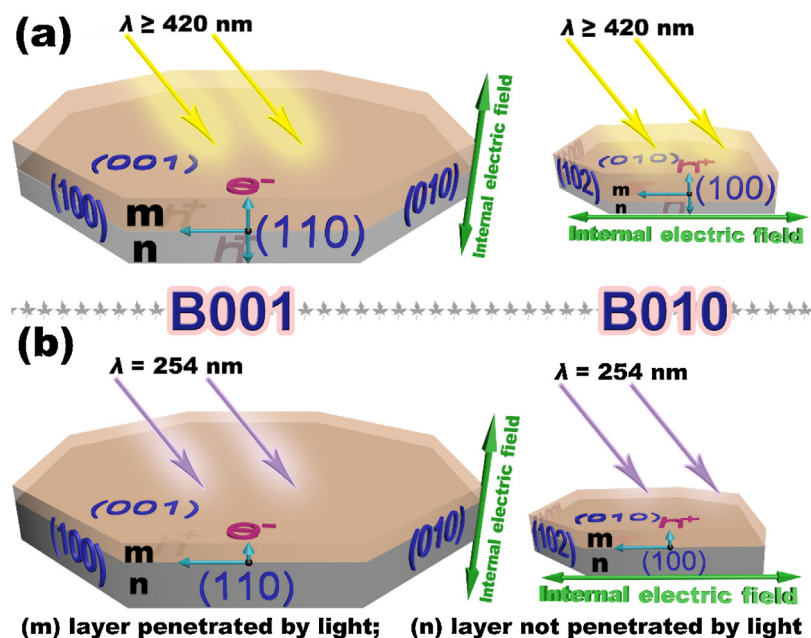
Fig. 8. Schematic illustrations of separation of photogenerated electrons (e^-) and holes (h^+) in the BiOBr nanosheets under light with different wavelengths (λ).

density than the B001. Under the VL420 and UV365 irradiations, the B010 exhibits higher photocatalytic performance than the B001 while a contrary result is observed under the UV254 irradiation. The λ-dependent photoactivity differences between the B010 and B001 arise from the differences in the H and $F(0\,0\,1)$ of the two BiOBr nanosheets. PL spectra and photocurrent results indicate that both the reduced H and increased $F(0\,0\,1)$ can accelerate the separation of photoinduced charge carriers and thus improve the photocatalytic activity. Whether the H or the $F(0\,0\,1)$ difference dominantly influences the photocatalytic activity of the B001 and B010 depends on the OPD of the incident light. This work systematically studies the relationship between the photocatalytic activity and the structure of the BiOBr nanosheets and will provides significant guidance for research on photocatalytic performance of 2D photocatalysts.

Acknowledgements

Appendix A. Supplementary data

Supplementary data associated with this article can be found, in the online version, at http://dx.doi.org/10.1016/j.apcatb.2016.01.053.

References

[1] D. Kim, K.K. Sakimoto, D. Hong, P. Yang, Angew. Chem. Int. Ed. 54 (2015) 3259–3266.
[2] C. Chen, W. Ma, J. Zhao, Chem. Soc. Rev. 39 (2010) 4206–4219.
[3] J.L. White, M.F. Baruch, J.E. Pander Iii, Y. Hu, I.C. Fortmeyer, J.E. Park, T. Zhang, K. Liao, J. Gu, Y. Yan, T.W. Shaw, E. Abelev, A.B. Bocarsly, Chem. Rev. 115 (2015) 12888–12935.
[4] S.J.A. Moniz, S.A. Shevlin, D.J. Martin, Z.-X. Guo, J. Tang, Energy Environ. Sci. 8 (2015) 731–759.
[5] Y. Zheng, L. Lin, B. Wang, X. Wang, Angew. Chem. Int. Ed. 54 (2015) 12868–12884.
[6] P. Zhou, J. Yu, M. Jaroniec, Adv. Mater. 26 (2014) 4920–4935.
[7] H. Xin, J.K. Katahara, I.L. Braly, H.W. Hillhouse, Adv. Energy Mater. 4 (2014), http://dx.doi.org/10.1002/aenm.201301823.
[8] H. Li, J. Liu, X. Liang, W. Hou, X. Tao, J. Mater. Chem. A 2 (2014) 8926–8932.
[9] H. Li, T. Hu, J. Liu, S. Song, N. Du, R. Zhang, W. Hou, Appl. Catal. B 182 (2016) 431–438.
[10] J. Zhu, F. Fan, R. Chen, H. An, Z. Feng, C. Li, Angew. Chem. Int. Ed. 54 (2015) 9111–9114.
[11] H. Li, Y. Sang, S. Chang, X. Huang, Y. Zhang, R. Yang, H. Jiang, H. Liu, Z.L. Wang, Nano Lett. 15 (2015) 2372–2379.
[12] K. Zhang, C. Liu, F. Huang, C. Zheng, W. Wang, Appl. Catal. B 68 (2006) 125–129.
[13] J. Li, Y. Yu, L. Zhang, Nanoscale 6 (2014) 8473–8488.
[14] H. Cheng, B. Huang, Y. Dai, Nanoscale 6 (2014) 2009–2026.
[15] H. Li, J. Shang, Z. Ai, L. Zhang, J. Am. Chem. Soc. 137 (2015) 6393–6399.
[16] G. Jiang, X. Wang, Z. Wei, X. Li, X. Xi, R. Hu, B. Tang, R. Wang, S. Wang, T. Wang, W. Chen, J. Mater. Chem. A 1 (2013) 2406.
[17] X. Zhang, L. Zhang, J. Phys. Chem. C 114 (2010) 18198–18206.
[18] L. Ye, J. Chen, L. Tian, J. Liu, T. Peng, K. Deng, L. Zan, Appl. Catal. B 130–131 (2013) 1–7.
[19] F. Dong, T. Xiong, Y. Sun, Y. Zhang, Y. Zhou, Chem. Commun. 51 (2015) 8249–8252.
[20] F.-t. Li, Q. Wang, J. Ran, Y.-j. Hao, X.-j. Wang, D. Zhao, S.Z. Qiao, Nanoscale 7 (2015) 1116–1126.
[21] D. Wu, B. Wang, W. Wang, T. An, G. Li, T.W. Ng, H.Y. Yip, C. Xiong, H.K. Lee, P.K. Wong, J. Mater. Chem. A 3 (2015) 15148–15155.
[22] M. Pan, H. Zhang, G. Gao, L. Liu, W. Chen, Environ. Sci. Technol. 49 (2015) 6240–6248.
[23] J. Jiang, K. Zhao, X. Xiao, L. Zhang, J. Am. Chem. Soc. 134 (2012) 4473–4476.
[24] H. Li, Q. Deng, J. Liu, W. Hou, N. Du, R. Zhang, X. Tao, Catal. Sci. Technol. 4 (2014) 1028–1037.
[25] W. Lin, X. Wang, Y. Wang, J. Zhang, Z. Lin, B. Zhang, F. Huang, Chem. Commun. (2014), http://dx.doi.org/10.1039/c1033cc41498a.
[26] M. Zhang, C. Shao, J. Mu, X. Huang, Z. Zhang, Z. Guo, P. Zhang, Y. Liu, J. Mater. Chem. 22 (2012) 577–584.
[27] Y. Huo, J. Zhang, M. Miao, Y. Jin, Appl. Catal. B 111–112 (2012) 334–341.
[28] L. Ye, L. Zan, L. Tian, T. Peng, J. Zhang, Chem. Commun. 47 (2011) 6951–6953.
[29] H. Li, J. Shi, K. Zhao, L. Zhang, Nanoscale 6 (2014) 14168–14173.
[30] Z. Zhang, C. Shao, X. Li, Y. Sun, M. Zhang, J. Mu, P. Zhang, Z. Guo, Y. Liu, Nanoscale 5 (2013) 606–618.
[31] M. Sathish, B. Viswanathan, R.P. Viswanath, C.S. Gopinath, Chem. Mater. 17 (2005) 6349–6353.
[32] C. Lv, G. Chen, J. Sun, Y. Zhou, S. Fan, C. Zhang, Appl. Catal. B 179 (2015) 54–60.
[33] K. Zhao, L. Zhang, J. Wang, Q. Li, W. He, J.J. Yin, J. Am. Chem. Soc. 135 (2013) 15750–15753.
[34] T. Lin, C. Yang, Z. Wang, H. Yin, X. Lü, F. Huang, J. Lin, X. Xie, M. Jiang, Energy Environ. Sci. 7 (2014) 967–972.
[35] J. Wang, Y. Yu, L. Zhang, Appl. Catal. B 136–137 (2013) 112–121.
[36] J. You, Z. Hong, Y. Yang, Q. Chen, M. Cai, T.-B. Song, C.-C. Chen, S. Lu, Y. Liu, H. Zhou, Y. Yang, ACS Nano 8 (2014) 1674–1680.
[37] X. Zhang, G. Ji, Y. Liu, X. Zhou, Y. Zhu, D. Shi, P. Zhang, X. Cao, B. Wang, Phys. Chem. Chem. Phys. 17 (2015) 8078–8086.
[38] J. You, Z. Hong, Y.M. Yang, Q. Chen, M. Cai, T.B. Song, C.C. Chen, S. Lu, Y. Liu, H. Zhou, Y. Yang, ACS Nano 8 (2014) 1674–1680.
[39] S. Poznyak, A. Kulak, Electrochim. Acta 35 (1990) 1941–1947.
[40] S. Yi, F. Zhao, X. Yue, D. Wang, Y. Lin, New J. Chem. 39 (2015) 6659–6666.
[41] L. Jing, W. Zhou, G. Tian, H. Fu, Chem. Soc. Rev. 42 (2013) 9509–9549.
[42] J.L. Gunjakar, I.Y. Kim, J.M. Lee, N.S. Lee, S.J. Hwang, Energy Environ. Sci. 6 (2013) 1008–1017.
[43] M. Stacey, Catal. Today 2 (1988) 621–631.
[44] H. Li, W. Hou, X. Tao, N. Du, Appl. Catal. B 172–173 (2015) 27–36.
[45] H. Li, J. Liu, W. Hou, N. Du, R. Zhang, X. Tao, Appl. Catal. B 160–161 (2014) 89–97.
[46] A. Hagfeldt, M. Graetzel, Chem. Rev. 95 (1995) 49–68.
[47] J. Yan, T. Wang, G. Wu, W. Dai, N. Guan, L. Li, J. Gong, Adv. Mater. 27 (2015) 1580–1586.
[48] H. Li, S. Gan, H. Wang, D. Han, L. Niu, Adv. Mater. 27 (2015) 6906–6913.
[49] F.E. Osterloh, Chem. Soc. Rev. 42 (2013) 2294–2320.
[50] L. Shi, L. Liang, F. Wang, J. Ma, J. Sun, Catal. Sci. Technol. 4 (2014) 3235–3243.
[51] Y.F. Joya, K.S. Joya, S. Bashir, A.W. Anwar, M.S. Rafique, R. Ahmed, Appl. Phys. A 120 (2015) 1173–1179.
[52] I.S. Jeong, J.H. Kim, S. Im, Appl. Phys. Lett. 83 (2003) 2946–2950.
[53] Y. Sheng-Hong, C. Sen, Y. Ning, Z. Yue-Li, Ferroelectrics 454 (2013) 78–83.
[54] N.M. Torkaman, Y. Ganjkhanlou, M. Kazemzad, H.H. Dabaghi, M. Keyanpour-Rad, Mater. Charact. 61 (2010) 362–370.
[55] H.A. Al-Khanbashi, W. Shirbeeny, A.A. Al-Ghamdi, L.M. Bronstein, W.E. Mahmoud, Spectrochim. Acta A 118 (2014) 800–805.